Quantifying local lattice distortions in refractory high-entropy alloys

(article starts on next page)

Quantifying local lattice distortions in refractory high-entropy alloys

Yao Hu (胡尧)[1], Lewis R. Owen[2], Helen Y. Playford[3], Aina Edgren[1],
Sheng Guo[4,*], and Magnus Hörnqvist Colliander[1,†]

[1]*Department of Physics, Chalmers University of Technology, Göteborg 41296, Sweden*
[2]*Department of Materials Science and Engineering, University of Sheffield, Sheffield S1 3JD, United Kingdom*
[3]*ISIS Neutron and Muon Source, STFC Rutherford Appleton Laboratory, Didcot OX11 0QX, United Kingdom*
[4]*Department of Industrial and Materials Science, Chalmers University of Technology, Göteborg 41296, Sweden*

Severe local lattice distortions (LLDs), originating from the size mismatch among atoms, have been proposed as one of the key mechanisms responsible for the excellent mechanical properties of bcc-structured high-entropy alloys (HEAs). They have also been connected to phase stability, as well as physical properties such as electrical conductivity. Experimental measurements of LLDs are, however, difficult and often ambiguous. Analysis of total scattering data in real space has been proposed to provide a uniquely suitable probe of LLDs, but its widespread application and validation are still limited. We conduct a thorough study of LLD measurements in refractory high-entropy alloys (RHEAs) using small-box pair distribution function (PDF) analysis. We start by reexamining existing literature data using a recently proposed coherent theoretical framework to demonstrate that LLDs in RHEAs can indeed be considered as severe and can be reliably measured even in the absence of known thermal components. We perform total scattering experiments of a typical RHEA (HfNbTaTiZr) using both x-rays and neutrons, and show that real-space PDF analysis of data from different types of radiation gives consistent values of LLDs. The results are also in good agreement with the values derived from reciprocal-space data. Finally, through simulation and analysis of theoretical two-phase PDFs, we demonstrate that the effect of the chemical segregation in the investigated RHEA on the measured LLDs is limited when dealing with comparatively large LLDs. The results show that PDF analysis using small-box modeling provides a fast and reliable tool for measuring LLDs in RHEAs, which makes it ideal for analysis of large data sets from time-resolved *in situ* measurements.

I. INTRODUCTION

High-entropy alloys (HEAs) have emerged as a promising class of metallic materials with unique properties that make them attractive for a wide range of applications. HEAs are essentially alloys that contain multiple principal elements in equiatomic or near-equiatomic proportions, resulting in a chemically disordered solid solution with high configurational entropy. As a result they are also commonly referred to as multiprincipal element alloys (MPEAs) or compositionally complex alloys (CCAs), although these terms are wider and include also alloys with medium configurational entropy. HEAs exhibit a number of interesting properties and have garnered significant interest in the metallurgical field in recent years [1,2]. Since HEAs were discovered in 2004 [3,4], the

field has exploded, with numerous studies of various properties of these materials and works to develop new HEAs with even more impressive characteristics [5]. One particularly interesting subset of HEAs comprises mainly refractory elements, specifically those from groups IV (Ti, Zr, Hf), V (V, Nb, Ta), and VI (Cr, Mo, W) [6,7]. These alloys, denoted refractory HEAs, or RHEAs [8], have received a lot of attention due to their exceptional high-temperature properties that surpass even the most advanced Ni-based superalloys at temperatures above 800–1000 °C [9].

One of the most notable features of HEAs is the presence of local lattice distortions (LLDs) [10], which are the static displacements of atoms from the ideal lattice sites, in order to accommodate the size differences among atoms. An estimate of the LLD is often obtained by considering the deviation of the atomic radii of the individual elements from the mean radius, the so-called atomic size mismatch

$$\delta = \sqrt{\sum_i c_i \left(1 - \frac{r_i}{\bar{r}}\right)^2}, \qquad (1)$$

where c_i and r_i are the concentration and atomic radius of element i, and $\bar{r} = \sum_i c_i r_i$ is the average atomic radius. While several studies have reported that LLDs in HEAs with face-centered cubic (fcc) crystal structure is negligibly larger than

---
*Contact author: sheng.guo@chalmers.se
†Contact author: magnus.colliander@chalmers.se

for those in dilute solid solutions [11,12], the body-centered cubic (bcc) structured RHEAs show much higher levels of LLDs [13]. It should be noted that estimates of LLDs in bcc-structured RHEAs, as derived from the parameter δ, can show significant discrepancies when compared to results from *ab initio* calculations or experimental observations [13,14]. These variances could be attributed to the fact that the atomic size mismatch is taken from an ideal hard sphere model, which inherently overlooks critical factors such as charge transfer effects that would be captured in density functional theory (DFT) and in experiments [15,16].

The most commonly discussed effect of LLDs on RHEAs is an enhanced solid solution strengthening [17–22]. Furthermore, in contrast to conventional bcc metals, some studies suggest that edge dislocations may play a role in controlling the plastic deformation of RHEAs [23–25], and there is emerging evidence that LLDs might impact the relative velocity of edge and screw dislocations [26]. In addition, *ab initio* calculations have also shown that LLDs play a fundamental role in the stability of the bcc phase, as the effect of the static displacement mimics dynamic thermal vibrations and thus effectively stabilizes the high-temperature stable bcc phase over the low-temperature stable hexagonal close-packed (hcp) structure [27]. Also physical properties such as electrical transport are affected by the extent of LLDs in RHEAs [28]. In addition to LLDs, short-range order (SRO) is also a significant feature of HEAs. While some studies have indicated that SRO is closely coupled with LLDs, both from microstructural observations [29] and from simulations [30], at least a computational study does suggest that SRO has only a minor inhibitory effect on LLD [31]. Currently, it is challenging to draw a definitive conclusion on the extent of influence from SRO on LLDs. Further quantitative investigations are needed to elucidate this relationship more clearly.

While extraction of LLDs from atomistic models is straightforward, experimental quantification remains a challenging task. The most common methods include transmission electron microscopy (TEM) [22,32,33], x-ray or neutron diffraction [34,35], extended x-ray absorption fine structure (EXAFS) [36,37], and total x-ray or neutron scattering [11,16,18,38,39]. Each technique has its advantages and disadvantages, recently reviewed by Owen and Jones [10]. An advantage of EXAFS and total scattering is that they provide direct access to the real-space pair distribution functions (PDFs), which facilitates a direct comparison to atomistic models. In comparison to EXAFS, total scattering is a bulk technique and produces PDFs over much larger distances to allow accurate fitting of the data. Large-box analysis of total scattering data, where the positions of several thousands of atoms are refined against experimental data through a reverse Monte Carlo algorithm [40–42], allows calculation of LLDs in a way analogous to atomistic simulations. It can therefore provide element-specific information, such as individual partial PDFs (which describe the distribution of distances between pairs of specific types of atoms in a multicomponent system) and preferred local neighborhoods (i.e., short-range order). Large-box modeling is, however, computationally expensive and time-consuming, and is therefore not well suited for analysis of large data sets with regard to the real-time feedback needs of *in situ* experiments. On the

other hand, small-box analysis based on the refinement of the structure described by a single unit cell (therefore often referred to as "real-space Rietveld") provides much shorter analysis time [43,44]. The limitation of small-box analysis lies in its inability to distinguish specific locations of individual atoms. Instead, it approximates the positions of atoms as a collective average. This is in contrast to the supercell approach in large-box analysis. The shorter analysis time becomes increasingly important as the development of rapid PDF acquisition techniques [45,46] has enabled time-resolved *in situ* measurements producing data volumes much too large to be effectively handled using large-box methods, as well as the promise of extensive improvements in time resolution at the new generation of spallation neutron sources such as European Spallation Source (ESS).

A further issue is the lack of consensus on the definition of LLDs (i.e., a suitable metric), and how it should be obtained from the experimental data. Recently, Owen and Jones reviewed the state-of-the-art of the field, and proposed a consistent terminology and interpretation [47]. As the long-range structure is maintained in the presence of LLDs (the average bond length must be consistent with the lattice parameter even though individual atoms experience static off-site displacements), the effect of variations in the local structure will result in a broader distribution of interatomic distances (bond lengths). This is indeed what is observed in *ab initio* studies [13,48,49]. Consequently, the width of the interatomic distance distribution, in relation to some reference distance, provides a measure of the local lattice strain, which can be compared between different material systems and experimental techniques.

As the peak width obtained from experimental measurements is a convolution of static (LLDs) and dynamic (thermal vibrations) displacements, separation of the two components is necessary. While the most accurate approach involves variable-temperature cryogenic measurements and allows fitting of the Debye curve [12], this is in many situations (e.g., *in situ* high-temperature measurements or when comparing multiple alloys) not experimentally feasible, as it is time-consuming. In such cases approximate estimations of the thermal contribution must be made.

In this study we focus on the use of small-box modeling for analysis of PDFs obtained from total scattering data. Through this approach we attempt to answer some questions regarding the extent of LLDs in RHEAs and their experimental characterization.

First, we consider the available literature data and examine the resulting magnitudes of LLDs derived from measurements of the atomic displacement parameter, U_{iso}, obtained from Rietveld refinements of diffraction measurements, and different assumptions made during the separation of static and thermal contributions. We conclude that LLDs in RHEAs are indeed significant (meaning, of the same order of magnitude as, or larger than, the thermal components), and their quantification is relatively robust with respect to approximate methods used to isolate the static displacements. This is promising for future studies, as it suggests that U_{iso}-based analysis without variable-temperature (cryogenic) measurements offers a sufficiently accurate way to measure LLDs, e.g., during time-resolved experiments.

Second, we examine one prototype material (gas atomized equiatomic HfNbTaTiZr) in more detail using both real-space and reciprocal-space refinements of synchrotron x-ray data, and compare the results to real-space analysis of neutron total scattering data for the same alloy. We confirm the severe LLDs derived from the literature data, and conclude that LLDs obtained from real-space and reciprocal-space analyses agree well, and that the results from x-ray and neutron experiments are consistent. The good agreement between the different techniques and probes confirms the robust nature of total scattering as a tool for LLD quantification.

Finally, we consider the effect of the chemical segregation observed in the HfNbTaTiZr RHEA powder on the accuracy of small-box based determination of LLDs. We perform single-phase small-box fitting of simulated two-phase PDFs describing of segregated structures, and conclude that for the investigated RHEA the LLDs can be accurately captured given the comparatively large magnitude of LLDs. This is, at least partially, due to the limited instrumental resolution in total scattering measurements masking the sample related broadening caused by the segregation.

II. LOCAL LATTICE DISTORTIONS IN RHEAs

A. Literature data and evaluation approach

In order to quantify the extent of LLDs in RHEA using the methods proposed in Introduction, the comprehensive data set presented by Tong *et al.* [14] was revisited. They performed an extensive characterization of several RHEAs using synchrotron diffraction and total scattering. For all alloys they reported values of the lattice parameter and U_{iso} obtained by Rietveld refinements and the magnitude of LLDs, quantified by a measure called ε_{1st} defined as

$$\varepsilon_{1st} = \frac{P_{1st} - P_{avg}}{P_{avg}}, \tag{2}$$

where P_{1st} is the position of the first peak in the real-space PDF (a measure of the local structure) and $P_{avg} = \sqrt{3}a/2$ is the expected position of the first peak calculated from the lattice parameter, a, from Rietveld refinements (average structure). For several alloys, in particular Zr and Hf containing variants, significant shifts of the first and second PDF peaks were observed, leading to large values of ε_{1st}. As can be seen from Fig. S1(a) in the Supplemental Material [50], no clear correlation between ε_{1st} and δ can be found.

However, ε_{1st} is an ambiguous measure as it also depends strongly on the relative scattering lengths of the different elements. Since the PDF is a histogram of interatomic distances weighted by the scattering lengths, the peak position will not correspond to the average bond length, but to the weighted bond length of different elemental pairs. Tong *et al.* used DFT to obtain relaxed structures, including LLDs, and PDFs calculated from the relaxed structures showed excellent agreement with the measured data. The results showed that there are significant deviations between the average position of AA, AB, and BB pairs (here A refers to Hf or Zr and B to other elements) obtained from DFT and P_{avg}. However, the average of all pairs agrees very well with the position calculated from the lattice parameter. This indeed indicates that the average

of the individual bond lengths (which would correspond to P_{1st} in the absence of weighting) do not differ significantly from P_{avg}, contrary to indications by ε_{1st}. On the other hand, the distribution of bond lengths was very broad as a result of the different average positions for AA, AB, and BB pairs, similar to previously reported *ab initio* [51] and hybrid Monte Carlo/molecular dynamics studies [52]. This suggests that this strain definition involving the position of the first peak in PDF might not be that appropriate for quantification of LLDs.

Here we therefore adopt the previously mentioned local lattice strain definition proposed by Owen and Jones [47], which is based on the width of the bond length distribution rather than the average bond length (peak position). In this framework, two different strain measures were proposed. The first is based on the magnitude of the static displacement away from the equilibrium position relative to the average atomic radius ($\bar{r}$). In the assumption of the hard-sphere model for bcc-structured RHEAs, $\bar{r}$ could be determined from the lattice parameter a, as

$$\bar{r} = \frac{\sqrt{3}}{4}a. \tag{3}$$

As the static displacements will be different for different local neighborhoods, the result will be a statistical distribution characterized by its standard deviation ($\sigma_{s,u}$). Here the subscript s indicates that it is the distribution of static (as opposed to thermal) displacements, and u indicates that it is the distribution of off-site displacements that is considered. The resulting lattice strain is given by

$$\varepsilon_{s,u} = \frac{\sigma_{s,u}}{\bar{r}}. \tag{4}$$

Alternatively, one can consider the statistical distribution of interatomic distances ($\sigma_{s,l}$, where l refers to bond length), relative to the average bond length (μ_l), according to

$$\varepsilon_{s,l} = \frac{\sigma_{s,l}}{\mu_l}. \tag{5}$$

The two are directly related as $\mu_l = 2\bar{r}$ in the hard-sphere approximation. Additionally, the standard deviation of the convoluted Gaussian distribution of interatomic distances of the atoms involved in a bond length measurement is given by $\sigma_{s,l} = \sqrt{2}\sigma_{s,u}$, due to the fact that the two atoms involved in the bond length measurement each have off-site displacements. The convoluted distribution has a variance equals to the sum of the variances of the off-site displacements distributions, which yields $\sigma_{s,l}^2 = \sigma_{s,u}^2 + \sigma_{s,u}^2$. Hence, $\sigma_{s,l} = \sqrt{2}\sigma_{s,u}$. This provides an upper limit given by $\varepsilon_{s,u} = \sqrt{2}\varepsilon_{s,l}$, assuming rigid bonds. In the following we have used $\varepsilon_{s,u}$ to represent the local lattice strain, as this allows the calculation of strain from the values of a and U_{iso} reported by Tong *et al.* [14]. Thus, σ_s and ε_s hereafter refer to $\sigma_{s,u}$ and $\varepsilon_{s,u}$, respectively.

B. Separating the thermal displacement

In diffraction and scattering experiments, the static displacements will be convoluted with dynamic (thermal) off-site displacements resulting from vibrations of atoms around their equilibrium positions, i.e., $\sigma^2 = \sigma_s^2 + \sigma_{th}^2$, where σ_{th} is the distribution of thermal displacements. In reciprocal space,

the off-site displacement of atoms leads to a Q-dependent decrease in the intensity of the Bragg peaks. This effect is accounted for by the Debye-Waller factor $\exp\{-\frac{1}{2}\sigma^2 Q^2\}$, where Q is the magnitude of the scattering vector. Rietveld refinements yield the atomic displacement parameter, denoted as $U_{iso} = \sigma^2$ in the case of isotropic displacements, which is typically assumed for metallic alloys. The above notation allows us to express U_{iso} as

$$U_{iso} = U_s + U_{th}, \qquad (6)$$

where $U_s = \sigma_s^2$ and $U_{th} = \sigma_{th}^2$. Subsequently, we have

$$\sigma_s = \sqrt{U_{iso} - U_{th}}. \qquad (7)$$

The same quantity, U_{iso}, can also be obtained from small-box analysis of PDF data acquired through total scattering experiments.

These techniques therefore measure the combined effect of thermal vibrations and LLDs, and to extract LLDs from the values of U_{iso} reported by Tong *et al.* [14] we must separate the static and thermal contributions. For individual elements (where $\sigma_s = 0$ by definition), $U_{th} = U_{iso}$ can be found from experimentally reported values of the Debye-Waller factors. The situation for alloys is more complicated, and the most accurate way is to perform temperature-dependent measurements at cryogenic temperatures. Here such measurements are not available, and we are restricted to estimating U_{th} from the available single-component values. The question which follows is how this can be reliably done?

The simplest way to estimate U_{th} from single-component values is to use the rule of mixtures (ROM) considering the individual values at the same temperature (T) as the test was performed

$$U_{th}^T = \sum_i c_i U_i^T, \qquad (8)$$

where c_i is the concentration and U_i^T the U_{iso} value of element i at temperature T. However, as pointed out by Owen *et al.* [11] the magnitude of the thermal vibrations resulting in U_{iso} depends on the bond strength, which in turn is related to the melting temperature. A slightly more elaborate estimation is thus to consider the U_i values at the same homologous temperature, $\tau = T/T_m$. If the melting temperature of the alloy ($T_{m,a}$) is known the homologous temperature for the alloy is given by

$$\tau_a = T/T_{m,a}, \qquad (9)$$

and U_{th} can be estimated as the average of the individual U_i values at the temperature corresponding to the same homologous temperature for each component as

$$U_{th}^\tau = \sum_i c_i U_i^\tau, \qquad (10)$$

where U_i^τ is the U_{iso} value of element i at temperature $T = \tau_a T_{m,i}$ and $T_{m,i}$ is the melting temperature of element i. However, the melting temperature of multicomponent alloys in general, and refractory versions in particular, is typically unknown and must also be estimated from the corresponding values of the individual components. Here two different methods were employed to estimate $T_{m,a}$ of the RHEAs in

Ref. [14]. The first approach involves the ROM to the values of $T_{m,i}$:

$$T_{m,a}^{ROM} = \sum_i c_i T_{m,i}. \qquad (11)$$

The second approach involves correcting the $T_{m,a}^{ROM}$ based on values determined by CALPHAD (CALculation of PHAse Diagrams) calculations. Senkov *et al.* [53] estimated the melting temperatures for a large number of RHEAs using CALPHAD. Although not all alloys investigated by Tong *et al.* were included in the calculations, Senkov *et al.* found an approximately linear relationship between the resulting $T_{m,a}^{CAL}$ (the value determined by CALPHAD) and $T_{m,a}^{ROM}$, indicating a robust correlation between them in spite of, e.g., eutectics, which allows us to perform a first-order correction. By only considering the alloys investigated in Ref. [53] involving the same elements as experimentally tested by Tong *et al.*, we establish the linear relationship between $T_{m,a}^{ROM}$ and $T_{m,a}^{CAL}$ (shown in Fig. S2 in the Supplemental Material [50]):

$$T_{m,a}^{CAL} = 1.28 T_{m,a}^{ROM} - 1043.5. \qquad (12)$$

Consequently, in addition to U_{th}^T, we now have two estimates of U_{th} based on the homologous temperature, U_{th}^{ROM} and U_{th}^{CAL}. Both are obtained from Eq. (10), but with τ_a calculated using $T_{m,a}$ from Eqs. (11) and (12), respectively.

In the subsequent calculations of U_{th} the values of $T_{m,i}$ were taken from Ref. [54], and values of U_i were obtained from temperature dependent values of the B factors of the individual elements reported in [55–57] as

$$U_i^T = \frac{B_i^T}{8\pi^2}, \qquad (13)$$

where B_i^T is the B factor of element i at temperature T. Note that values of U_i^T are only reported at temperatures up to room temperature, but as the melting temperature for the elements involved is high the values of $\tau_a T_{m,i}$ are typically close to room temperature, thus linear inter- and extrapolation can be safely used (see Fig. S3 in the Supplemental Material [50]). All the calculation results are listed in Table S I in the Supplemental Material [50].

Figure 1 shows a comparison of the different approaches, where the obtained values of U_{th}^{ROM} and U_{th}^{CAL} are plotted against U_{th}^{RT} [U_{th}^T according to Eq. (8) with $T = 293$ K] for the different alloys investigated in Tong *et al.* [14]. While U_{th}^{ROM} generally aligns well with U_{th}^{RT} and consistently remains lower, the values of U_{th}^{CAL} are increasingly higher than those of U_{th}^{RT}, with a few exceptions. However, the difference between different methods is relatively small, which indicates that the choice of method for estimating U_{th} is not critical. Nevertheless, the discrepancy increases and care should be taken for alloys where the calculated U_{th} is high (above around 0.005 Å^2). Here we chose U_{th}^{CAL} in the subsequent analysis, as it provides the most conservative estimate of the static contributions (i.e., the smallest LLDs).

C. Local lattice strains in RHEAs

With estimates of U_{th} available, we can now separate the static and thermal contributions from the values of U_{iso} for the different alloys investigated in Tong *et al.* [14]. The results
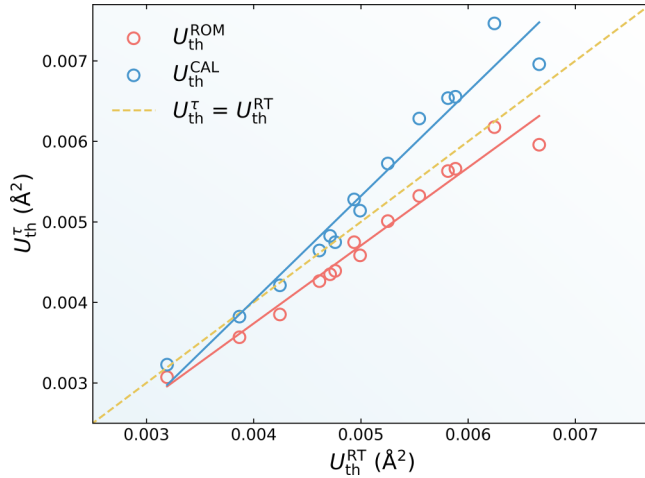
FIG. 1. Comparison between different methods of evaluating thermal components of U_{iso} from various RHEAs. The solid lines are linear fits for respective methods.

are shown in Fig. 2, where it can be clearly seen that the static contributions are of the same order or larger than the thermal components. This is in stark contrast to the case for fcc-structured HEAs [12] and confirms that the local lattice distortions in bcc-structured RHEAs can indeed be considered to be severe. The values of the resulting local lattice strains, ε_s, are tabulated in Table I, together with the thermal strains ($\varepsilon_{th} = \sqrt{U_{th}}/\bar{r}$ [47]), along with U_{iso} and ε_{1st} reported by Tong *et al.* [14] for comparison. While most of the alloys (those without Zr) have values of ε_s ranging from 4.08% to 6.85% (average $5.85 \pm 1.0\%$), the Zr-containing alloys exhibit very large values, around 10%. While ε_s and δ are not directly comparable in the presence of charge transfer effects, we note
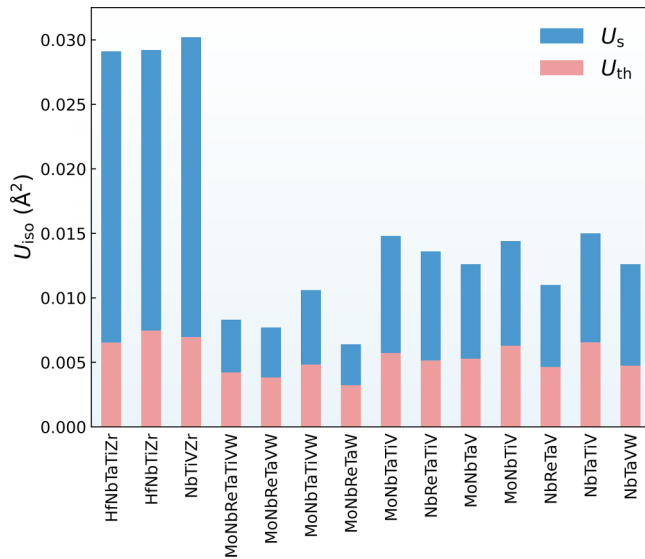

FIG. 2. Static (U_s) and thermal (U_{th}) components of off-site displacements (U_{iso}) extracted from several RHEAs [14]. Thermal displacements calculated from a linear extrapolation model (described in Sec. II B) and total U_{iso} determined experimentally by Tong *et al.* [14] from diffraction data. The relatively larger magnitude of U_s than U_{th} indicates that LLDs in bcc-structured RHEAs are severe.

that these ε_s values (10.18%, 9.91%, and 10.61%) are well above the previously proposed stability limit of crystalline solid solutions in HEAs ($\delta \leqslant 6.6\%$) [59]. We also note that there appears to be a strong correlation between the chemical composition and ε_s, whereas there is a poor correlation between ε_{1st} and the composition. Comparing MoNbTaV and MoNbTiV, where the only difference is the exchange of Ti for Ta, the value of ε_{1st} changes drastically, from 0.65% to 0.01%. The value of ε_s, on the other hand, is relatively similar (6.18% compared to 6.53%), which is more in line with expectations. The large change in ε_{1st} is potentially explained by the previously discussed fact that the peak position is affected by weighting of the scattering lengths. The negative scattering length of Ti (compared to the positive values for the other elements, except V, which has a slightly negative value, see Table SIII in the Supplemental Material [50]) can be expected to have a large effect. This is supported by the fact that the effect of exchanging W for Ti in NbTaVW has a similar effect (ε_{1st} changes largely from 0.32% to 0.82%, whereas ε_s changes slightly from 6.39% to 6.57%). Similarly, HfNbTaTiZr and HfNbTiZr (differing only in the presence of Ta in the former) have similar values of ε_s but very different ε_{1st}. While the addition or removal of Hf and Zr is expected to significantly affect LLDs due to the extensive charge transfer and associated change in effective size [14–16], Ta is not expected to have the same effect. We also note that the resulting values of ε_s do not show any consistent correlation with δ or ε_{1st}; see Figs. S1(b) and S1(c) in the Supplemental Material [50]. As mentioned earlier, the reason that there is no observable correlation between ε_s and δ is that the charge transfer effect has not been accounted for in the r_i values used for δ.

In summary, we have compared different methods to estimate the thermal contribution to U_{iso} obtained from diffraction or scattering experiments based on single-component values, and found that the choice of method did not have a significant effect. Isolating the static contribution allowed calculation of the local lattice strains from the values of U_{iso} reported for several RHEAs in Ref. [14]. The results show that LLDs in bcc-structured RHEAs are indeed severe, in contrast to fcc-structured HEAs.

III. LLDs IN HfNbTaTiZr FROM TOTAL SCATTERING AND DIFFRACTION

In the previous section we calculated ε_s from U_{iso} values obtained from Rietveld refinement of x-ray diffraction data. It has, however, been argued that values of U_{iso} obtained from total scattering measurements should be more reliable [60]. In this part we perform x-ray total scattering measurements of the HfNbTaTiZr RHEA powder to allow a comparison of ε_s derived from reciprocal- and real-space refinements. This alloy was chosen as it has very large LLD (Table I). Furthermore, we perform neutron total scattering measurements of the same alloy in order to investigate the effect of the radiation type, as the scattering lengths which provide the weighting in the PDFs are different for x-rays and neutrons, and the neutron scattering lengths are Q-independent (in contrast to the case for x-rays).

TABLE I. Values of static (ε_s) and recalculated thermal (ε_{th}) strains from Sec. II B, as well as their ratio ($\varepsilon_s/\varepsilon_{th}$), along with U_{iso} and LLDs (ε_{1st}) from the literature, and atomic size mismatch (δ).

Composition	ε_s (%)	ε_{th} (%)	$\varepsilon_s/\varepsilon_{th}$	U_{iso}[†] (Å^2)	ε_{1st}[†] (%)	δ[*] (%)
HfNbTaTiZr	10.18	5.48	1.86	0.0291	0.91	4.03
HfNbTiZr	9.91	5.81	1.71	0.0292	0.39	4.32
NbTiVZr	10.61	5.81	1.83	0.0302	2.00	5.16
MoNbReTaTiVW	4.66	4.73	0.99	0.0083	0.08	3.30
MoNbReTaVW	4.54	4.51	1.01	0.0077	0.23	3.57
MoNbTaTiVW	5.50	5.03	1.09	0.0106	0.21	3.21
MoNbReTaW	4.08	4.11	0.99	0.0064	0.05	3.47
MoNbTaTiV	6.85	5.44	1.26	0.0148	0.52	2.80
NbReTaTiV	6.67	5.20	1.28	0.0136	0.02	3.21
MoNbTaV	6.18	5.24	1.18	0.0126	0.65	3.23
MoNbTiV	6.53	5.75	1.14	0.0144	0.01	2.94
NbReTaV	5.80	4.96	1.17	0.0110	0.22	3.57
NbTaTiV	6.57	5.78	1.14	0.0150	0.82	2.95
NbTaVW	6.39	4.97	1.29	0.0126	0.32	3.57
Nb	0	5.42	0	0.0060	–	–

[†]From Ref. [14].

[*]Calculated based on Eq. (1), with r_i from Ref. [58].

A. Materials and methods

1. Material

HfNbTaTiZr was obtained in the form of gas atomized powders. Ingots of the initial HfNbTaTiZr alloy were prepared by arc-melting of blends of pure metals with >99.9 wt% purity placed in a water-cooled copper crucible, under protective helium atmosphere. To mix the elements in the melt pool properly and to homogenize the produced material, the ingot was flipped and repeatedly remelted (eight times). The ingots were subsequently gas atomized into powder by electrode induction-melting gas atomization in a crucible-free process under protective Ar atmosphere to suppress undesirable oxidation of the material. The particle size distribution of the powder is 17–277 µm (Dv10-Dv90). Every powder particle contains numerous equiaxed grains, and the average diameter of these grains is 9.5 ± 2.9 µm [61]. The microstructure of the powder was characterized using energy-dispersive x-ray spectroscopy (EDS) in a scanning electron microscope (FEI Quanta 200 FEG ESEM operated at 10 kV). Back-scatter electron (BSE) imaging was performed at 10 kV to obtain high-resolution chemical contrast. A BSE image of the microstructure and the corresponding EDS maps are shown in Fig. 3. A dendritic microstructure can be clearly observed, indicating the presence of chemical segregation within the material. This is similar to the as-cast material investigated by Tong *et al.* [14]. The chemical composition was determined by EDS analysis and listed in Table II. The bulk values were derived from averaging two map scans, while the dendrite and interdendrite values were obtained from point scans, averaging 10 and 9 points, respectively. Significant variations in elemental composition are observed between dendrites and interdendritic regions, with enrichment of Nb and Ta in the dendrites, while Hf, Ti, and Zr with relatively lower melting points are more abundant in the interdendritic regions. The partitioning is the same as reported by Tong *et al.* [14] (and other studies [61,62]), but the magnitude of the chemical differences is larger in the present material due to the rapid
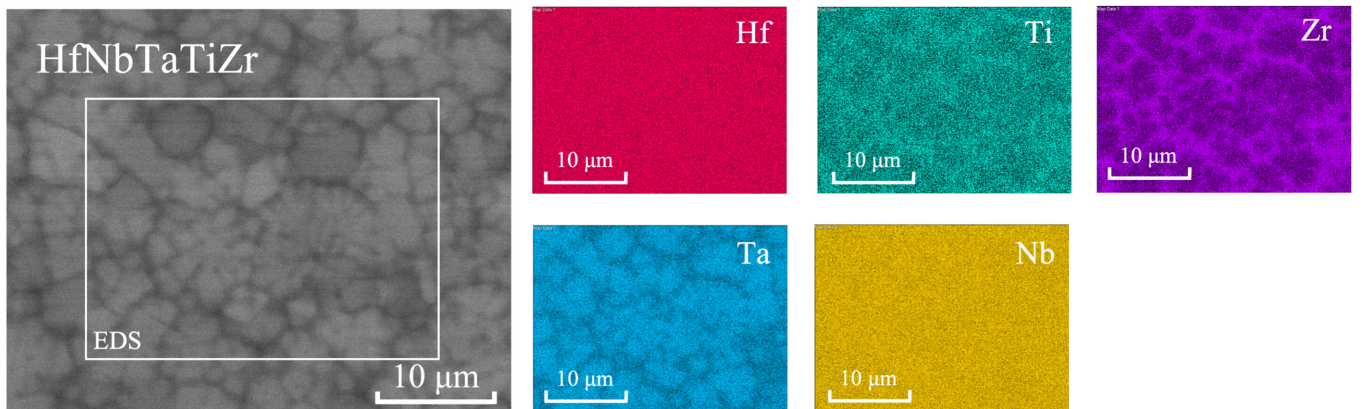

FIG. 3. Dendritic microstructure of a HfNbTaTiZr powder sample showed by SEM and EDS.

TABLE II. Chemical composition in atomic percent (at.%) of HfNbTaTiZr from EDS.

Element	Hf	Nb	Ta	Ti	Zr
Bulk	20.49(6)	19.0(2)	20.3(5)	22.3(2)	17.9(5)
Dendrite	19.0(3)	21.6(4)	27.9(6)	18.8(5)	12.7(4)
Interdendrite	21.0(4)	15.1(6)	11(1)	27.4(8)	25(1)

solidification associated with the gas atomization process. The effect of the segregation on the measured U_{iso}, and hence ε_s, will be discussed in Sec. IV.

2. Experimental methods

Synchrotron total scattering data was collected at P02.1 DESY, Germany [63], at an energy of 59.8 keV using a downstream VAREX XRD 4343CT area detector at a distance of 0.301 m (calibrated using NIST 660c LaB$_6$ powder). Quartz glass capillaries with diameter of 1 mm were used to contain the powder sample, and background measurements were performed. The data were reduced and transformed to PDF using PDFgetX3 [64] with $Q_{max} = 21.04$ Å^{-1}.

A high-resolution synchrotron diffraction experiment was performed at the P21.2 beamline at PETRA III (DESY, Hamburg, Germany) at an energy of 82 keV with the powder contained in 1 mm quartz glass capillaries. A combination of a high-resolution monochromator (a four-bounce channel-cut Si 111 producing an energy resolution of 10^{-4}) and a multi-detector setup (four VAREX XRD 4343CT detectors to cover a sufficient Q-range while maintaining a sample-to-detector distance of 2.94 m in transmission to optimize the resolution) was used.

Neutron total scattering data were collected on the GEM diffractometer at the ISIS Neutron and Muon Source, Rutherford Appleton Laboratory, UK [65,66]. Five one-hour measurements were carried out at room temperature for the HfNbTaTiZr powder mounted in a vanadium can. The raw total scattering data were reduced using GudrunN software [67] ($Q_{max} = 34$ Å^{-1}) to remove instrument and container backgrounds. The GudrunN software calculates an attenuation correction as part of the data reduction process to account for neutrons absorbed by Hf. The wavelength range used to generate the $F(Q)$ (reduced total scattering structure function) and subsequently the $G(r)$ (reduced pair distribution function) was 0.36–3.55 Å, hence the Hf resonance at 0.273 Å was avoided. Instrument and container backgrounds were measured separately, and Fourier transformed into PDFs for subsequent analysis. Identical measurements were performed on pure Nb powder for reference.

3. Data analysis

To obtain LLDs from the reciprocal-space x-ray data, a 1D diffractogram was obtained using PyFAI 22.0 [68]. Rietveld refinement was performed using GSAS-II software [69], with an instrument file derived from the LaB$_6$ standard. As explained in Sec. II B, static displacements will result in an increased value of U_{iso}. This is manifested by a more rapid decrease in the intensity with Q, which is captured by the atomic form factor

$$f = f_0 \exp\left(-\tfrac{1}{2}U_{iso}Q^2\right) \tag{14}$$

in the refinement (f and f_0 are atomic form factors at a particular momentum transfer Q and zero momentum transfer, respectively). During the refinements the lattice parameter a, U_{iso} and microstrain were used. U_{iso} was constrained to be the same for all atoms in the unit cell, which was represented by a bcc structure (I$m\bar{3}m$) with fractional occupancy corresponding to the average alloy composition from the EDS measurement (Table II). The inclusion of microstrain was necessary to obtain good fits, presumably due to the broad distribution of lattice parameters originating from the varying chemistry across dendrites and interdendritic regions (this will be further discussed in Sec. IV), but also as the sample is an as-atomized sample, there is likely to be a reasonably high dislocation density in the particles that have not necessarily been removed by heat treating. The choice of microstrain broadening, rather than size broadening, is arbitrary since we are only attempting to obtain a more accurate peak profile, and not a physical interpretation to the refined value.

For real-space data, small-box analysis of the PDFs was performed in PDFgui software [43,70]. In PDFgui, the peak width (σ) is modeled as

$$\sigma(r) = \sqrt{U_{iso}\left(1 - \frac{\delta_1}{r} - \frac{\delta_2}{r^2} + Q_{broad}^2 r^2\right)}, \tag{15}$$

where δ_1 and δ_2 are used to account for narrowing of the peaks at small r due to correlated motion (here only δ_2 was used, i.e., $\delta_1 = 0$ as the temperature is low [71]), and Q_{broad} accounts for PDF peak broadening from increased intensity noise at high Q. It should be noted that there is also broadening from the reciprocal-space peak shape effect, as detailed in Sec. V of the Supplemental Material [50]. While a, U_{iso}, and δ_2 were refined, the values of Q_{broad} and Q_{damp} (which describes the dampening of the PDF peak in real space due to instrument resolution) were determined by fitting the PDF from the reference (LaB$_6$ in the case of x-rays and Nb in the case of neutrons). The PDFs were fitted in the range $r \leqslant 20$ Å, as this range is relatively robust to artifacts induced by instrumental resolution [72].

In all cases LLDs were calculated based on Eqs. (3), (4), and (7), as

$$\varepsilon_s = \frac{\sqrt{U_{iso} - U_{th}}}{\frac{\sqrt{3}}{4}a}, \tag{16}$$

where $U_{th} = 0.0065$ Å^2 was determined for the HfNbTaTiZr alloy in Sec. II.

B. Results

The peak intensities in the x-ray diffractogram (Fig. 4) exhibits a significant decay with increasing Q, consistent with the observations by Tong *et al.* [14]. This can be attributed to the combined effects of the LLDs, thermal vibrations and x-ray form factor decay as previously discussed. Figure 4 also shows the results of the Rietveld refinement, and the obtained parameters are tabulated in Table III. The local lattice strain is 6.53%, which is significantly smaller than the value obtained from U_{iso} reported by Tong *et al.* [14] (10.18%, see Table I). By examining the fitting of the PDF in Fig. 5(a)
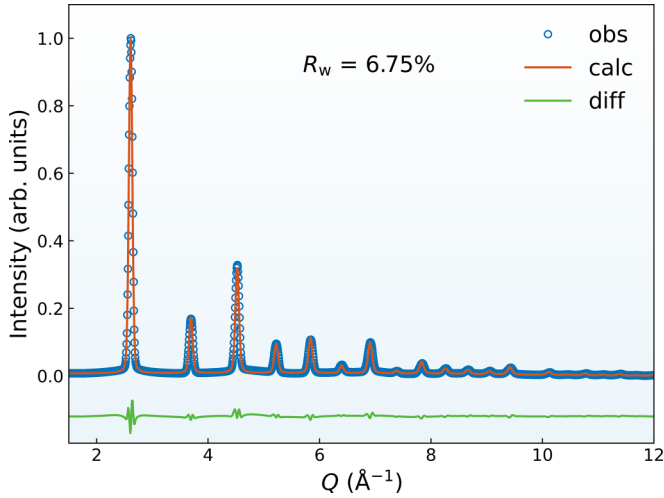
FIG. 4. The x-ray diffractogram, including results from Rietveld refinement of HfNbTaTiZr. R_w is the overall weighted profile R factor as a statistical measure to quantify the difference between the observed and calculated x-ray diffraction patterns.

[to avoid confusion, here the term PDF refers to the reduced pair distribution function, $G(r)$, as defined in, e.g., [73]], a pronounced difference at the first-nearest-neighbor (1NN) and the second-nearest-neighbor (2NN) peaks can be observed [more clearly shown in Fig. 5(b)], which again is consistent with Ref. [14]. The resulting values of U_{iso} and ε_s are shown in Table III and are consistent with the results from the reciprocal-space analysis ($\varepsilon_s = 7.76\%$ for real-space data, slightly higher than the value obtained from the reciprocal-space data $\varepsilon_s = 6.53\%$). The obtained lattice parameter agrees well with that obtained from the Rietveld refinement.

The result of the small-box analysis of the neutron PDF is shown in Figs. 5(c) and 5(d), and tabulated in Table III. The value of ε_s is 7.16%, intermediate between the reciprocal and real-space analysis of the x-ray data. Again, the lattice parameter is consistent with the results from x-ray data analysis.

It should also be noted that although the current small-box analysis was performed with Q_{damp} and Q_{broad} fixed to the instrumental values, allowing them to be refined did not significantly affect the resulting value of U_s (an effect of less than 10%, see Table SII in the Supplemental Material [50]). Neither did excluding the region containing the 1NN and 2NN peaks, the positions of which are shifted and could affect the

TABLE III. Comparison of lattice parameters (a), off-site displacement parameters (U_{iso}), and local lattice strain (ε_s) for the HfNbTaTiZr RHEA from reciprocal-space and real-space (PDF) analysis of synchrotron and neutron data.

	x-ray		Neutron
	Diffraction	PDF	PDF
a (Å)	3.4019(1)	3.4010(8)	3.4041(6)
U_{iso} (Å^2)	0.0158(2)	0.0197(6)	0.0168(4)
ε_s (%)	6.53	7.76	7.16

fitting as they will have the largest effect on δ_2, which in turn is correlated with U_{iso} [74].

In summary, we find a good agreement between real-space (PDF) and reciprocal-space (diffraction) analysis of x-ray scattering data, which is also consistent with results from neutron PDF analysis. The latter indicates that the effect of radiation type is negligible, even in the case where Ti (which has a negative scattering length for neutrons but positive for x-rays) is included in the composition. All obtained values of LLDs are significantly smaller than those derived from the previously reported U_{iso} values in Ref. [14], although the microstructure of the alloys are qualitatively similar. The reason for this discrepancy is not known at this stage.

IV. INVESTIGATING ERRORS

One question which arises from the investigation in Sec. III is whether or not the inhomogeneous structure resulting from the chemical segregation will significantly affect the results of the small-box analysis, which is based on a single unit cell. This is an important aspect, as many potential applications of RHEAs could involve materials in their as-cast state, which shows similarly segregated structures [6,7,14]. As homogenization treatments of these materials must be performed at very high temperatures and/or long times, there will certainly be components and applications where this is not practically possible. Thus, an understanding of LLDs also in segregated structures is important. To address these issues, we use the DiffPy-CMI modeling framework [70]. This allows generation of PDFs from a material described by crystal structure, lattice parameter, fractional occupancy, and U_{iso}, convoluted with instrumental effects (more details will be presented later). Using DiffPy-CMI we generate theoretical multiphase PDFs to simulate the microstructure of our HfNbTaTiZr RHEA, which are then fitted using a single-phase model to characterize the error.

A. High-resolution diffraction analysis of segregated HfNbTaTiZr

To generate realistic PDFs the chemistry, lattice parameter, and phase fractions of the "two phases" (dendrites and interdendritic regions) are required. While the chemistry is found from the EDS measurements in Table II, the lattice parameters and phase fractions can be obtained by Rietveld refinement of the high-resolution synchrotron x-ray diffraction data, which supports the presence of a "two-phase" structure, is presented in Fig. 6. The data were refined using two bcc phases with scattering lengths determined from the chemistry of the dendrites and interdendritic regions given by the EDS measurements (the calculation of the scattering lengths of individual elements from [75] are listed in Table SIII in the Supplemental Material [50], together with the resulting average scattering lengths for the two regions). We refined the lattice parameters and microstrains for the individual phases, as well as U_{iso}, which was constrained to be the same for both dendrites and interdendritic regions, and the volume fraction.

Figure 6(a) shows the 110 peak, where a broad asymmetric shape is seen due to the segregation. The data are well described by a two-phase refinement [Fig. 6(b)]
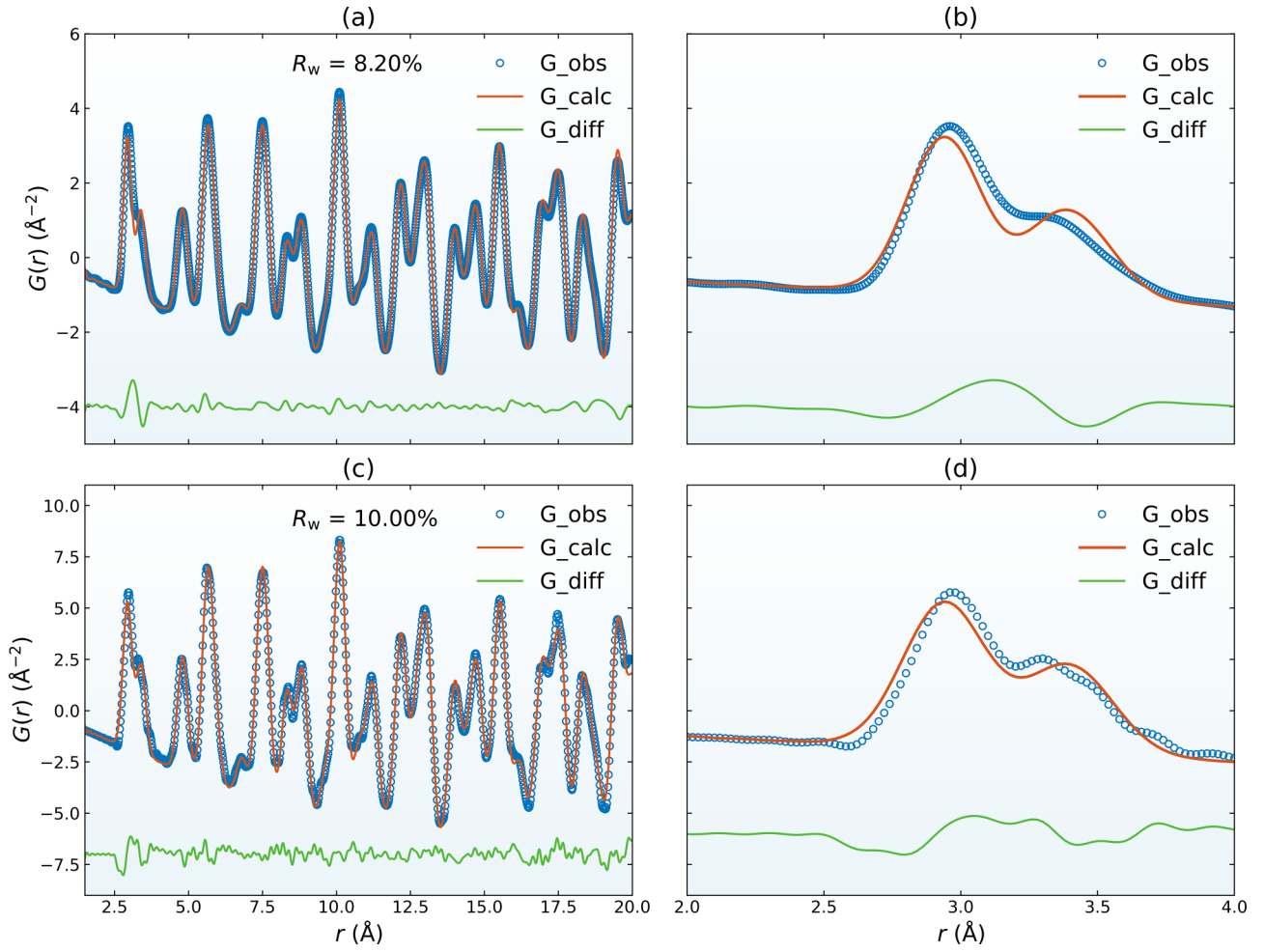
FIG. 5. (a) The x-ray PDF including small-box fitting result of HfNbTaTiZr. (b) Enlarged view of the 1NN and 2NN in the x-ray PDF. (c) The neutron PDF including small-box fitting result of HfNbTaTiZr. (b) Enlarged view of the 1NN and 2NN in the neutron PDF.
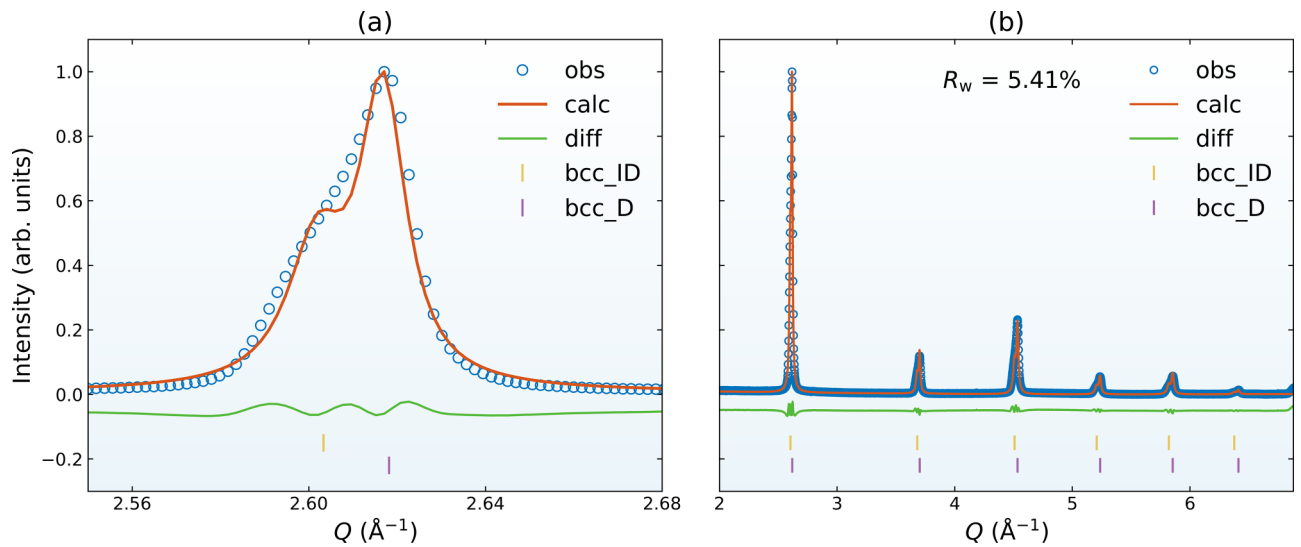

FIG. 6. (a) Magnified view of the 110 peak. (b) The high-resolution x-ray diffractogram, including results from the two-phase Rietveld refinement of HfNbTaTiZr.

resulting in $a_D = 3.3938(1)$ Å (the lattice parameter of dendrites), $a_{ID} = 3.4129(2)$ Å (the lattice parameter of interdendritic regions) and a volume fraction of interdendritic regions of $V_F = 0.47(1)$, which is in good agreement with the volume fraction derived from the partitioning of alloying elements, 0.44 (see Fig. S4 in the Supplemental Material [50]). Examining the fit in more detail, the refined peak profiles are sharper than the experimental peaks (in Fig. 6(a) the experimental data appear like a broad asymmetric peak, whereas the refinement exhibit two distinct, although overlapping, peaks), presumably due to the fact that the dendrites and interdendritic regions are not distinct phases, but rather regions with different average composition. In reality the composition varies continuously in the microstructure, leading to much broader distributions of the lattice parameter than can be captured using the microstrain parameter. With the lattice parameters and volume fraction values of the two phases available, we can simulate two-phase PDFs. We also note that the value of $U_{iso} = 0.0156(4)$ Å^2 (and consequently the local lattice strain $\varepsilon_s = 6.46\%$) from the refinement of the high-resolution diffraction data is consistent with the values from the single-phase analysis above ($U_{iso} = 0.0158(2)$ Å^2 from x-ray diffraction data in Table III).

B. Simulation

Here we define the multiphase based on the segregation shown in Sec. III A 1. As mentioned earlier, while a segregated microstructure consists of continuous modulations of the chemistry, it can for simplicity be viewed as being composed of two phases, dendrites (D) and interdendritic regions (ID), with different chemistry and consequently different lattice parameters. According to Ref. [76] the PDF of a multiphase system can be expressed as the weighted sum of the PDFs [expressed as $G(r)$]:

$$G(r) = \sum_p w_p G_p(r), \qquad (17)$$

where w_p is the wight and $G_p(r)$ is the PDF of phase p. The weights are given by

$$w_p = x_p \frac{\bar{b}_p^2}{\sum_p x_p \bar{b}_p^2}, \qquad (18)$$

where x_p is the molar fraction and $\bar{b}_p$ is the average scattering length

$$\bar{b}_p = \sum_i c_{i,p} b_{i,p}. \qquad (19)$$

$c_{i,p}$ and $b_{i,p}$ are the concentration and scattering length, respectively, of element i in phase p.

Using this approach we generated a theoretical neutron PDF corresponding to our RHEA, consisting of a mix of dendrites ($a_D = 3.3938$ Å) and interdendritic regions ($a_{ID} = 3.4129$ Å), with a phase fraction of interdendritic regions $V_F = 0.47$. We assume that LLDs (U_s) are the same in both phases, and set $U_{iso}^{sim} = U_s^{sim} + U_{th}^{sim} = 0.0103 + 0.0065 = 0.0168$ Å^2 from the single-phase fitting of the neutron PDF data (see Table III). This is reasonable also from a physical standpoint, since the actual difference must be small in

chemically similar and structurally identical regions, and the effects of small changes in U_s do not significantly affect the PDF. The values of instrument-related parameters were the same as those obtained from fitting the neutron PDF of Nb in Sec. III (i.e., the instrumental effect should be representative of a typical total scattering beamline at a neutron source), and the value of δ_2 (describing the correlated motion) was obtained from the fit of the neutron PDF for HfNbTaTiZr, again as described in Sec. III. All parameters are listed in Table SIV in the Supplemental Material [50].

The two-phase PDF was then compared with a single-phase PDF, simulated the same parameters except for the lattice parameter $a = 3.4041$ Å derived from neutron PDF experiment (Table III). The comparison of the two simulated PDFs were shown in Fig. 7(a), where it is evident that the discrepancy between the PDF from homogeneous microstructure (single-phase) and the PDF from segregated microstructure (two-phase) is minimal. This suggests that the chemical segregation has a negligible effect on the PDF in our alloy and that the single-phase analysis in Sec. III is reasonably accurate. The error can be quantified by fitting the two-phase PDF with a single-phase model, allowing only a and U_{iso} to vary, in order to extract U_s in a way analogous to our previous analysis of HfNbTaTiZr. The resulting values of the fitting parameters (a_{fit} and U_{iso}^{fit}) were used to calculate the local lattice strain applying Eq. (16):

$$\varepsilon_{fit} = \frac{\sqrt{U_{iso}^{fit} - U_{th}^{sim}}}{a_{fit} \cdot \frac{\sqrt{3}}{4}}. \qquad (20)$$

This can be compared to the true local lattice strain:

$$\varepsilon_{sim} = \frac{\sqrt{U_s^{sim}}}{\bar{r}_{sim}} = \frac{\sqrt{U_s^{sim}}}{\bar{a}_{sim} \cdot \frac{\sqrt{3}}{4}}, \qquad (21)$$

where

$$\bar{a}_{sim} = (1 - V_F)a_1 + V_F a_2 \qquad (22)$$

is the average lattice parameter of the two-phase structure (the exact value of the lattice parameter does not have a significant effect on the result, which is dominated by differences in U). The difference between the fitted and the true values of the local lattice strains

$$\eta = \frac{\varepsilon_{fit} - \varepsilon_{sim}}{\varepsilon_{sim}} \qquad (23)$$

is a measure of the error induced by fitting the two-phase (segregated) structure with a single-phase model. In this way we obtain an error in the value of ε_s determined by fitting a two-phase PDF with a single-phase model of around 3%.

However, it can be expected that the error will depend on the magnitude of the LLDs, as the PDFs from the individual phases will become more distinctly separated as the peak width decreases. We therefore varied the static displacement in the simulation, U_s^{sim} from 0 to 0.0235 Å^2, resulting in $0.0065 \leqslant U_{iso}^{sim} = U_s^{sim} + U_{th}^{sim} \leqslant 0.03$. Each two-phase PDF was then fitted as described above, and the resulting error η calculated.

When η is plotted against U_s^{sim} in Fig. 7(b), the error increases as the level of LLDs (U_s^{sim}) decreases, confirming the expected inverse correlation between them. For values of
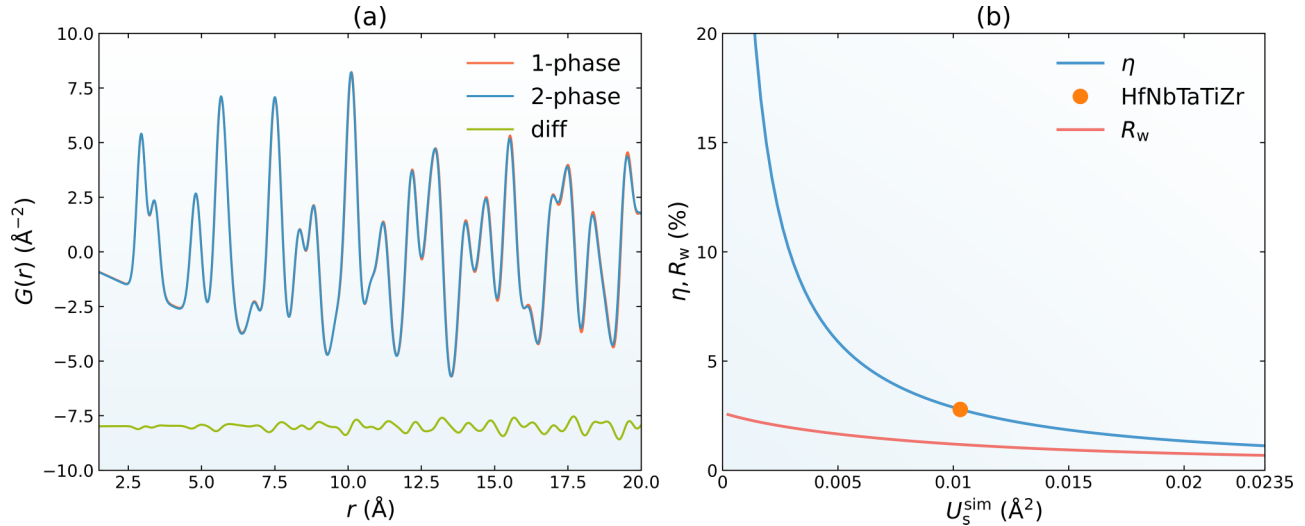
FIG. 7. (a) Comparison of simulated PDFs for the HfNbTaTiZr alloy in homogeneous (single-phase) and segregated (two-phase) microstructures. (b) The error (η) distribution of LLDs from single-phase PDF analysis of simulated PDFs, with respect to the magnitude of LLDs (U_s^{sim}). The orange point denotes the HfNbTaTiZr alloy applying the U_{iso} value from neutron PDF data. R_w is the weighted profile R factor from the fits.

U_{iso} larger than around 0.003 Å^2, the error in ε_s is smaller than 10%, which is probably sufficient for most purposes. For smaller LLDs, the error increases rapidly, indicating that care must be taken. We also note that the error will depend on the difference between the lattice parameter between the different regions, as an increased difference will lead to an increased separation of the peaks in the PDF. Consequently, the results obtained here are only valid for the specific alloy and segregation level investigated in this study. In the low-U_s region, fitting the data with a two-phase model could provide a better option, as the individual contributions should become more easily separable. In order to examine the potential of the latter approach for materials with large LLDs, we attempted to fit our experimental data with a two-phase model, but this did not give significantly different results from the single-phase fit (see Sec. IX in the Supplemental Material [50]). This is consistent with the low values of R_w in Fig. 7(b), which is due to the lack of clear separation of the contributions from the two phases, even at $U_s^{sim} = 0$, due to the small lattice parameter difference.

C. Instrumental resolution

The reason for the very limited impact of the segregated structure on the PDF analysis is the relatively low instrumental resolution, which is a result of the small sample-to-detector distance required to achieve a sufficiently high Q range. Figure 8(a) shows a comparison of the 110 peak from the RHEA and the 111 peak from the LaB$_6$ standard (located at approximately the same Q) from both the total scattering experiment and the high-resolution diffraction measurement. It can be seen that the broad instrument profile in the case of total scattering (TS, dark red and dark blue) is hardly affected by the convolution with the sample, whereas there is a significant peak broadening in the case of the high-resolution measurement. As the reciprocal-space peak width will affect both

damping and width of the PDF peaks [72,74,77,78], sample-related reciprocal-space peak broadening will directly impact the real-space peak widths (for further discussion see Sec. V in the Supplemental Material [50]), i.e., the value of U_{iso}. As the sample related reciprocal-space broadening is small in the total scattering experiment, so is the effect on U_{iso}. This also explains the insensitivity of U_{iso} to whether Q_{damp} and Q_{broad} are refined or not, as discussed in Sec. V in the Supplemental Material [50]. We note that while small-box modeling has limited possibilities to include reciprocal-space peak shape in the analysis, large-box modeling has been shown to be able to handle arbitrary peak shapes in the refinements [79].

In the case of time-of-flight neutron total scattering measurements, the reciprocal-space data used in the transformation to real space is collected by several different detector banks placed at different scattering angles. As the Q-space resolution increases with increasing scattering angle, the banks will have different resolution. In Fig. 8(b) we compare the 211 peak of both RHEA and Nb from a low-angle bank (Bank 3) and a high-angle bank (Bank 6). The effect of sample broadening is more pronounced in the high-angle (high-resolution) bank compared to the low-angle (low-resolution) bank. As precise PDFs should include as wide a Q range as possible, banks with different resolutions are combined and subtle features within the sample, e.g., chemical segregation, which is sensitive to the peak widths, could be lost.

V. CONCLUSION

The use of total scattering for measuring LLDs in bcc-structured RHEAs has been explored. In conclusion, we have shown the following:

(1) LLDs in bcc-structured RHEAs can be reliably characterized by real-space small-box PDF analysis of total scattering data. The static lattice strains are of the same order, or larger than, the thermal components. Consequently LLDs
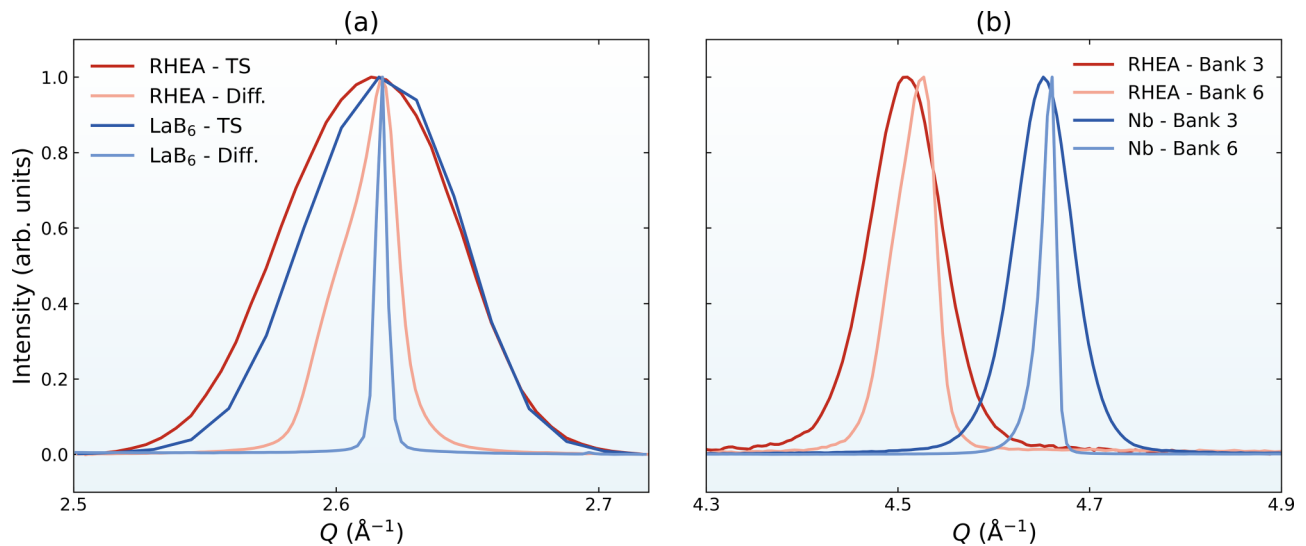
FIG. 8. (a) A comparison between x-ray total scattering and high-resolution diffraction pattern of the RHEA HfNbTaTiZr and LaB$_6$ standard (normalized by maximum intensity). A more significant sample-related peak broadening was observed in high-resolution diffraction experiment (denoted "Diff." in the legend), compared to the total scattering experiments ("TS"), due to the much better instrumental resolution resolving the dendrites and interdendritic regions. (b) A comparison between neutron total scattering pattern of Bank 3 (low scattering angle) and Bank 6 (high scattering angle) from GEM diffractometer at ISIS of the RHEA HfNbTaTiZr and Nb (normalized by maximum intensity).

in these alloys can be classified as severe, unlike some of the studied fcc counterparts.

(2) Real-space analysis of PDF data from x-ray and neutron total scattering measurements gave consistent values of LLDs in HfNbTaTiZr RHEA, which in turn agreed with analysis of reciprocal-space data.

(3) Single-phase small-box modeling of chemically segregated (two-phase) microstructures provides reliable LLD values. Through analysis of theoretical data sets we have provided a means of assessing the error associated with fitting a segregated structure with a single-phase models, and shown that effect is negligible of our HfNbTaTiZr RHEA.

The results show that PDF analysis using small-box modeling provides a fast and reliable tool for measuring LLDs in RHEAs, which makes it ideal for analysis of large data sets from time-resolved *in situ* measurements.

ACKNOWLEDGMENTS

[1] E. P. George, D. Raabe, and R. O. Ritchie, High-entropy alloys, Nat. Rev. Mater. **4**, 515 (2019).

[2] D. B. Miracle and O. N. Senkov, A critical review of high entropy alloys and related concepts, Acta Mater. **122**, 448 (2017).

[3] J. W. Yeh, S. K. Chen, S. J. Lin, J. Y. Gan, T. S. Chin, T. T. Shun, C. H. Tsau, and S. Y. Chang, Nanostructured high-entropy alloys with multiple principal elements: Novel alloy design concepts and outcomes, Adv. Eng. Mater. **6**, 299 (2004).

[4] B. Cantor, I. T. Chang, P. Knight, and A. J. Vincent, Microstructural development in equiatomic multicomponent alloys, Mater. Sci. Eng. A **375–377**, 213 (2004).

[5] J. W. Yeh, Alloy design strategies and future trends in high-entropy alloys, JOM **65**, 1759 (2013).

[6] O. N. Senkov, G. B. Wilks, D. B. Miracle, C. P. Chuang, and P. K. Liaw, Refractory high-entropy alloys, Intermetallics **18**, 1758 (2010).

[7] S. Sheikh, S. Shafeie, Q. Hu, J. Ahlström, C. Persson, J. Veselý, J. Zýka, U. Klement, and S. Guo, Alloy design for intrinsically ductile refractory high-entropy alloys, J. Appl. Phys. **120**, 164902 (2016).

[8] O. N. Senkov, D. B. Miracle, K. J. Chaput, and J. P. Couzinie, Development and exploration of refractory high entropy alloys—A review, J. Mater. Res. **33**, 3092 (2018).

[9] O. N. Senkov, G. B. Wilks, J. M. Scott, and D. B. Miracle, Mechanical properties of Nb25Mo25Ta 25W25 and V20Nb20Mo 20Ta20W20 refractory high entropy alloys, Intermetallics **19**, 698 (2011).

[10] L. R. Owen and N. G. Jones, Lattice distortions in high-entropy alloys, J. Mater. Res. **33**, 2954 (2018).

[11] L. R. Owen, E. J. Pickering, H. Y. Playford, H. J. Stone, M. G. Tucker, and N. G. Jones, An assessment of the lattice strain in the CrMnFeCoNi high-entropy alloy, Acta Mater. **122**, 11 (2017).

[12] L. Owen, N. Jones, H. Stone, and H. Playford, Separation of static and dynamic displacements in the CrMnFeCoNi high entropy alloy, Acta Mater. **262**, 119164 (2024).

[13] H. Song, F. Tian, Q. M. Hu, L. Vitos, Y. Wang, J. Shen, and N. Chen, Local lattice distortion in high-entropy alloys, Phys. Rev. Mater. **1**, 023404 (2017).

[14] Y. Tong, S. Zhao, H. Bei, T. Egami, Y. Zhang, and F. Zhang, Severe local lattice distortion in Zr- and/or Hf-containing refractory multi-principal element alloys, Acta Mater. **183**, 172 (2020).

[15] L. Casillas-Trujillo, B. Osinger, R. Lindblad, D. Karlsson, A. I. Abrikosov, S. Fritze, K. Von Fieandt, B. Alling, I. Hotz, U. Jansson, I. A. Abrikosov, and E. Lewin, Experimental and theoretical evidence of charge transfer in multi-component alloys-how chemical interactions reduce atomic size mismatch, Mater. Chem. Front. **5**, 5746 (2021).

[16] F. Meng, W. Zhang, Z. Zhou, R. Sheng, A. C. Chuang, C. Wu, H. Huang, S. Zhang, H. Zhang, L. Zhu, L. Jiang, P. K. Liaw, S. Chen, and Y. Tong, Charge transfer effect on local lattice distortion in a HfNbTiZr high entropy alloy, Scr. Mater. **203**, 114104 (2021).

[17] Z. Wang, Q. Fang, J. Li, B. Liu, and Y. Liu, Effect of lattice distortion on solid solution strengthening of BCC high-entropy alloys, J. Mater. Sci. Technol. **34**, 349 (2018).

[18] P. Thirathipviwat, S. Sato, G. Song, J. Bednarcik, K. Nielsch, J. Jung, and J. Han, A role of atomic size misfit in lattice distortion and solid solution strengthening of TiNbHfTaZr high entropy alloy system, Scr. Mater. **210**, 114470 (2022).

[19] S. I. Rao, C. Varvenne, C. Woodward, T. A. Parthasarathy, D. Miracle, O. N. Senkov, and W. A. Curtin, Atomistic simulations of dislocations in a model BCC multicomponent concentrated solid solution alloy, Acta Mater. **125**, 311 (2017).

[20] Y. Y. Zhao, Z. F. Lei, Z. P. Lu, J. C. Huang, and T. G. Nieh, A simplified model connecting lattice distortion with friction stress of nb-based equiatomic high-entropy alloys, Mater. Res. Lett. **7**, 340 (2019).

[21] C. Lee, G. Song, M. C. Gao, R. Feng, P. Chen, J. Brechtl, Y. Chen, K. An, W. Guo, J. D. Poplawsky, S. Li, A. T. Samaei, W. Chen, A. Hu, H. Choo, and P. K. Liaw, Lattice distortion in a strong and ductile refractory high-entropy alloy, Acta Mater. **160**, 158 (2018).

[22] C. Lee, Y. Chou, G. Kim, M. C. Gao, K. An, J. Brechtl, C. Zhang, W. Chen, J. D. Poplawsky, G. Song, Y. Ren, Y. C. Chou,

and P. K. Liaw, Lattice-distortion-enhanced yield strength in a refractory high-entropy alloy, Adv. Mater. **32**, 2004029 (2020).

[23] B. Chen, S. Li, H. Zong, X. Ding, J. Sun, and E. Ma, Unusual activated processes controlling dislocation motion in body-centered-cubic high-entropy alloys, Proc. Natl. Acad. Sci. USA **117**, 16199 (2020).

[24] C. Lee, F. Maresca, R. Feng, Y. C. Chou, T. Ungar, M. Widom, K. An, J. D. Poplawsky, Y. C. Chou, P. K. Liaw, and W. A. Curtin, Strength can be controlled by edge dislocations in refractory high-entropy alloys, Nat. Commun. **12**, 5474 (2021).

[25] F. Wang, G. H. Balbus, S. Xu, Y. Su, J. Shin, P. F. Rottmann, K. E. Knipling, J.-C. Stinville, L. H. Mills, O. N. Senkov, I. J. Beyerlein, T. M. Pollock, and D. S. Gianola, Multiplicity of dislocation pathways in a refractory multiprincipal element alloy, Science **370**, 95 (2020).

[26] B. Chen, S. Li, J. Ding, X. Ding, J. Sun, and E. Ma, Correlating dislocation mobility with local lattice distortion in refractory multi-principal element alloys, Scr. Mater. **222**, 115048 (2023).

[27] G. D. Samolyuk, Y. N. Osetsky, G. M. Stocks, and J. R. Morris, Role of static displacements in stabilizing body centered cubic high entropy alloys, Phys. Rev. Lett. **126**, 025501 (2021).

[28] S. Mu, S. Wimmer, S. Mankovsky, H. Ebert, and G. M. Stocks, Influence of local lattice distortions on electrical transport of refractory high entropy alloys, Scr. Mater. **170**, 189 (2019).

[29] R. Zhang, S. Zhao, J. Ding, Y. Chong, T. Jia, C. Ophus, M. Asta, R. O. Ritchie, and A. M. Minor, Short-range order and its impact on the CrCoNi medium-entropy alloy, Nature (London) **581**, 283 (2020).

[30] Q. He, P. Tang, H. Chen, S. Lan, J. Wang, J. Luan, M. Du, Y. Liu, C. Liu, C. Pao, and Y. Yang, Understanding chemical short-range ordering/demixing coupled with lattice distortion in solid solution high entropy alloys, Acta Mater. **216**, 117140 (2021).

[31] X. Zhou, H. Song, C. Guo, Z. Yang, and F. Tian, Effect of short-range order on lattice distortion, stacking fault energy, and mechanical performance of Co-Fe-Ni-Ti high-entropy alloy at finite temperature, Phys. Rev. Mater. **8**, 053602 (2024).

[32] Y. Zou, S. Maiti, W. Steurer, and R. Spolenak, Size-dependent plasticity in an $Nb_{25}Mo_{25}Ta_{25}W_{25}$ refractory high-entropy alloy, Acta Mater. **65**, 85 (2014).

[33] A. Béché, J. L. Rouvière, J. P. Barnes, and D. Cooper, Dark field electron holography for strain measurement, Ultramicroscopy **111**, 227 (2011).

[34] J. W. Yeh, S. Y. Chang, Y. D. Hong, S. K. Chen, and S. J. Lin, Anomalous decrease in x-ray diffraction intensities of Cu-Ni-Al-Co-Cr-Fe-Si alloy systems with multi-principal elements, Mater. Chem. Phys. **103**, 41 (2007).

[35] N. L. Okamoto, K. Yuge, K. Tanaka, H. Inui, and E. P. George, Atomic displacement in the CrMnFeCoNi high-entropy alloy— A scaling factor to predict solid solution strengthening, AIP Adv. **6**, 125008 (2016).

[36] A. Fantin, A. M. Manzoni, H. Springer, R. D. Kamachali, and R. Maaß, Local lattice distortions and chemical short-range order in MoNbTaW, Mater. Res. Lett. **12**, 346 (2024).

[37] Y. Y. Tan, T. Li, Y. Chen, Z. J. Chen, M. Y. Su, J. Zhang, Y. Gong, T. Wu, H. Y. Wang, and L. H. Dai, Uncovering heterogeneity of local lattice distortion in TiZrHfNbTa refractory high entropy alloy by SR-XRD and EXAFS, Scr. Mater. **223**, 115079 (2023).

[38] L. R. Owen, H. J. Stone, and H. Y. Playford, The assessment of local lattice strains in alloys using total scattering, Acta Mater. **170**, 38 (2019).

[39] M. M. Nygård, W. A. Sławiński, G. Ek, M. H. Sørby, M. Sahlberg, D. A. Keen, and B. C. Hauback, Local order in high-entropy alloys and associated deuterides—A total scattering and Reverse Monte Carlo study, Acta Mater. **199**, 504 (2020).

[40] M. G. Tucker, D. A. Keen, M. T. Dove, A. L. Goodwin, and Q. Hui, RMCProfile: Reverse Monte Carlo for polycrystalline materials, J. Phys.: Condens. Matter **19**, 335218 (2007).

[41] H. Y. Playford, L. R. Owen, I. Levin, and M. G. Tucker, New insights into complex materials using reverse Monte Carlo modeling, Annu. Rev. Mater. Res. **44**, 429 (2014).

[42] H. Playford, D. Keen, and M. Tucker, Local structure of crystalline and amorphous materials using reverse Monte Carlo methods, Neutron News **27**, 17 (2016).

[43] C. L. Farrow, P. Juhas, J. W. Liu, D. Bryndin, E. S. Boin, J. Bloch, T. Proffen, and S. J. Billinge, PDFfit2 and PDFgui: Computer programs for studying nanostructure in crystals, J. Phys.: Condens. Matter **19**, 335219 (2007).

[44] S. J. L. Billinge, Real-space Rietveld: Full profile structural refinement of the atomic pair distribution function, in *Local Structure from Diffraction*, edited by S. J. L. Billinge and M. F. Thorpe, Fundamental Materials Research (Springer, Boston, MA, 2002), pp. 137–156.

[45] P. J. Chupas, X. Qiu, J. C. Hanson, P. L. Lee, C. P. Grey, and S. J. L. Billinge, Rapid-acquisition pair distribution function (RA-PDF) analysis, J. Appl. Cryst. **36**, 1342 (2003).

[46] P. J. Chupas, K. W. Chapman, and P. L. Lee, Applications of an amorphous silicon-based area detector for high-resolution, high-sensitivity and fast time-resolved pair distribution function measurements, J. Appl. Cryst. **40**, 463 (2007).

[47] L. R. Owen and N. G. Jones, Quantifying local lattice distortions in alloys, Scr. Mater. **187**, 428 (2020).

[48] L. Y. Tian, G. Wang, J. S. Harris, D. L. Irving, J. Zhao, and L. Vitos, Alloying effect on the elastic properties of refractory high-entropy alloys, Mater. Des. **114**, 243 (2017).

[49] H. Ge and F. Tian, A review of ab initio calculation on lattice distortion in high-entropy alloys, JOM **71**, 4225 (2019).

[50] See Supplemental Material at http://link.aps.org/supplemental/10.1103/PhysRevMaterials.8.083602 for correlation between different LLD metrics; determination of the relationship between melting temperatures derived from rule-of-mixture and CALPHAD; calculated thermal component of U_{iso} values for a range of RHEAs; tabulation of B factors of pure elements; an extended discussion of the effect of reciprocal-space peak broadening on the PDF; calculations of average scattering lengths for dendrites and interdendritic regions; a list of parameters used in PDF simulations; calulations of volume fractions of dendrites and interdendritic regions from the lever rule; and description of two-phase small-box fitting procedure.

[51] X. T. Chen, L. Shao, T. W. Fan, N. Ding, J. Yang, and B. Y. Tang, Ab initio study of local lattice distortion of hexagonal closed-packed high-entropy $(Mo_{0.25}Nb_{0.25}Ta_{0.25}V_{0.25})(Al_{0.5}Si_{0.5})_2$ and the influence on thermodynamic property, J. Solid State Chem. **303**, 122469 (2021).

[52] M. Widom, W. P. Huhn, S. Maiti, and W. Steurer, Hybrid Monte Carlo/molecular dynamics simulation of a refractory metal high entropy alloy, Metall. Mater. Trans. A **45**, 196 (2014).

[53] O. N. Senkov, S. Gorsse, and D. B. Miracle, High temperature strength of refractory complex concentrated alloys, Acta Mater. **175**, 394 (2019).

[54] *Handbook of Physics*, edited by W. Benenson, J. W. Harris, H. Stocker, and H. Lutz (Springer, New York, NY, 2002).

[55] L. M. Peng, G. Ren, S. L. Dudarev, and M. J. Whelan, Debye-Waller factors and absorptive scattering factors of elemental crystals, Acta Cryst. A **52**, 456 (1996).

[56] M. S. Narayana, N. G. Krishna, and D. B. Sirdeshmukh, X-ray determination of Debye–Waller factors and Debye temperatures of h.c.p. elements Ti, Zr, Ru, Tm, Hf, Acta Cryst. A **57**, 217 (2001).

[57] E. Purushotham and N. G. Krishna, Mean square amplitudes of vibration and associated Debye temperatures of rhenium, osmium and thallium, Phys. B: Condens. Matter **405**, 3308 (2010).

[58] J. C. Slater, Atomic radii in crystals, J. Chem. Phys. **41**, 3199 (1964).

[59] X. Yang and Y. Zhang, Prediction of high-entropy stabilized solid-solution in multi-component alloys, Mater. Chem. Phys. **132**, 233 (2012).

[60] E. Takeshi and S. J. L. Billinge, Structure of complex materials, Pergamon Mater. Ser. **16**, 1 (2012).

[61] F. Lukac, M. Dudr, R. Musalek, J. Klecka, J. Cinert, J. Cizek, T. Chraska, J. Cizek, O. Melikhova, J. Kuriplach, J. Zyka, and J. Malek, Spark plasma sintering of gas atomized high-entropy alloy HfNbTaTiZr, J. Mater. Res. **33**, 3247 (2018).

[62] S. Y. Chen, Y. Tong, K. K. Tseng, J. W. Yeh, J. D. Poplawsky, J. G. Wen, M. C. Gao, G. Kim, W. Chen, Y. Ren, R. Feng, W. D. Li, and P. K. Liaw, Phase transformations of HfNbTaTiZr high-entropy alloy at intermediate temperatures, Scr. Mater. **158**, 50 (2019).

[63] A. C. Dippel, H. P. Liermann, J. T. Delitz, P. Walter, H. Schulte-Schrepping, O. H. Seeck, and H. Franz, Beamline P02.1 at PETRA III for high-resolution and high-energy powder diffraction, J. Synchrotron Radiat. **22**, 675 (2015).

[64] P. Juhás, T. Davis, C. L. Farrow, and S. J. L. Billinge, PDFgetX3: A rapid and highly automatable program for processing powder diffraction data into total scattering pair distribution functions, J. Appl. Cryst. **46**, 560 (2013).

[65] W. G. Williams, R. M. Ibberson, P. Day, and J. E. Enderby, GEM—General materials diffractometer at ISIS, Phys. B: Condens. Matter **241–243**, 234 (1997).

[66] A. C. Hannon, Results on disordered materials from the General materials diffractometer, GEM, at ISIS, Nucl. Instrum. Methods Phys. Res. Sect. A **551**, 88 (2005).

[67] A. K. Soper, GudrunN and GudrunX: Programs for correcting raw neutron and x-ray diffraction data to differential scattering cross section, RAL technical report RAL-TR-2011-013, 1 (2011).

[68] J. Kieffer, V. Valls, N. Blanc, and C. Hennig, New tools for calibrating diffraction setups, J. Synchrotron Radiat. **27**, 558 (2020).

[69] B. H. Toby and R. B. Von Dreele, GSAS-II: The genesis of a modern open-source all purpose crystallography software package, J. Appl. Cryst. **46**, 544 (2013).

[70] P. Juhás, C. L. Farrow, X. Yang, K. R. Knox, and S. J. Billinge, Complex modeling: A strategy and software program for combining multiple information sources to solve ill posed structure

and nanostructure inverse problems, Acta Cryst. A **71**, 562 (2015).

[71] I.-K. Jeong, R. H. Heffner, M. J. Graf, and S. J. L. Billinge, Lattice dynamics and correlated atomic motion from the atomic pair distribution function, Phys. Rev. B **67**, 104301 (2003).

[72] D. Olds, C. N. Saunders, M. Peters, T. Proffen, J. Neuefeind, and K. Page, Precise implications for real-space pair distribution function modeling of effects intrinsic to modern time-of-flight neutron diffractometers, Acta Cryst. A **74**, 293 (2018).

[73] P. F. Peterson, D. Olds, M. T. McDonnell, and K. Page, Illustrated formalisms for total scattering data: A guide for new practitioners, J. Appl. Cryst. **54**, 317 (2021).

[74] I. K. Jeong, M. J. Graf, and R. H. Heffner, Effects of Bragg peak profiles and nanoparticle sizes on the real-space pair distribution function, J. Appl. Cryst. **38**, 55 (2005).

[75] V. F. Sears, Neutron scattering lengths and cross sections, Neutron News **3**, 26 (1992).

[76] W. A. Sławiński, Calculation of pair distribution functions for multiphase systems, J. Appl. Cryst. **51**, 919 (2018).

[77] X. Qiu, E. S. Božin, P. Juhas, T. Proffen, and S. J. Billinge, Reciprocal-space instrumental effects on the real-space neutron atomic pair distribution function, J. Appl. Cryst. **37**, 110 (2004).

[78] J. Beyer, N. Roth, and B. Brummerstedt Iversen, Effects of Voigt diffraction peak profiles on the pair distribution function, Acta Cryst. A **78**, 10 (2022).

[79] Y. Zhang, M. Eremenko, V. Krayzman, M. G. Tucker, and I. Levin, New capabilities for enhancement of *RMCProfile*: Instrumental profiles with arbitrary peak shapes for structural refinements using the reverse Monte Carlo method, J. Appl. Cryst. **53**, 1509 (2020).

[80] https://doi.org/10.5286/ISIS.E.RB2000207